Advanced Composites and Hybrid Materials (2025) 8:81
https://doi.org/10.1007/s42114-024-01153-5

RESEARCH

Engineered Cu-VT composite nanoparticles induce copper-dependent cell death in bladder cancer: insights from single-cell spatial transcriptomics

Fangdie Ye[1,2] · Chen Ye[3] · Yufeng Zhao[4] · Weijian Li[1,2] · Jinhao Zhang[1,2] · Yuxi Ou[1,2] · Ziang Chen[1,2] · Zhang Cheng[1,2] · Jing Zhang[5] · Shujaat Ali[6] · Omer Salman Qureshi[6] · Yufei Liu[1,2] · Xiangpeng Dai[7,8] · Hang Huang[9] · Haowen Jiang[1,2,10]

Received: 8 July 2024 / Revised: 22 November 2024 / Accepted: 9 December 2024

Abstract

Bladder cancer (BLCA), particularly due to the high recurrence and progression rates of non-muscle-invasive bladder cancer (NMIBC), is a significant global health challenge. Current treatments, such as Bacillus Calmette-Guérin (BCG) immunotherapy and intravesical chemotherapy, often cause substantial side effects and exhibit limited efficacy, highlighting the urgent need for novel therapeutic strategies. Single-cell spatial transcriptomic advancements have identified cuproptosis as a critical pathway in BLCA, presenting a promising target for treatment. In this study, these insights were leveraged to design Cu-VT nanoparticles (NPs), an innovative composite material that combines the unique properties of copper ions and the natural flavonoid vitexin, to induce cuproptosis. Cu-VT NPs could effectively induce apoptosis and oxidative stress in BLCA cells concurrently modulating the immune response within the tumor microenvironment. Comprehensive in vitro and in vivo experiments demonstrated that Cu-VT NPs significantly inhibited tumor growth and reduced lung metastasis through cuproptosis induction. This dual-function composite material enhances therapeutic efficacy and minimizes side effects, showcasing its potential as a revolutionary treatment for BLCA. Our findings highlight the transformative potential of Cu-VT NPs in the context of BLCA treatment, establishing a new paradigm in the use of composite materials for the treatment of advanced cancer.

Keywords Bladder cancer · Nanoparticles · Cuproptosis · Transcriptomics · Vitexin

Fangdie Ye, Chen Ye, and Yufeng Zhao contributed equally in this article.

✉ Yufei Liu
chosenlyf@hotmail.com

✉ Xiangpeng Dai
daixiangpeng@jlu.edu.cn

✉ Hang Huang
huanghang2017@163.com

✉ Haowen Jiang
urology_hshan@163.com

[1] Department of Urology, Huashan Hospital, Fudan University, Shanghai, China

[2] Fudan Institute of Urology, Huashan Hospital, Fudan University, Shanghai, China

[3] Department of Urology, Changhai Hospital, Second Military Medical University, Shanghai 200433, China

[4] Department of Urology, Zhongshan Hospital, Fudan University, Shanghai, China

[5] Division of Basic Biomedical Sciences, The University of South Dakota Sanford School of Medicine, Vermillion, SD 57069, USA

[6] Department of Pharmacy, Forman Christian College (A Chartered University), Lahore, Pakistan

[7] Key Laboratory of Organ Regeneration and Transplantation of Ministry of Education, First Hospital of Jilin University, Changchun, China

[8] National-Local Joint Engineering Laboratory of Animal Models for Human Disease First Hospital of Jilin University, Changchun, China

[9] Department of Urology, The First Affiliated Hospital of Wenzhou Medical University, Wenzhou City, China

[10] National Clinical Research Center for Aging and Medicine, Huashan Hospital, Fudan University, Shanghai, China

Published online: 24 December 2024

1 Introduction

Bladder cancer (BLCA) continues to be a major global health continues. Upon initial diagnosis, around 75% of cases are of non-muscle-invasive bladder cancer (NMIBC) [1]. While NMIBC is less likely to invade the muscle layer, it has high recurrence and progression rates. Standard treatments for this condition include intravesical immunotherapy and chemotherapy [2]. A common immunotherapy, Bacillus Calmette-Guérin (BCG), induces a local immune response to reduce tumor recurrence [3]. However, BCG can lead to adverse effects such as bladder irritation, urinary tract infections, and systemic reactions, sometimes leading to treatment discontinuation [4]. Likewise, intravesical chemotherapy agents like mitomycin C are used for the treatment of NMIBC, killing cancer cells and inhibiting their proliferation [5]. Nonetheless, these agents come with toxicities, including cystitis, urethral stricture, and bone marrow suppression, adding significant burdens to the treatment. Despite improving NMIBC prognosis, the limited efficacy and significant side effects of treatments render BLCA as one of the most expensive cancers to manage [6]. The emergence of drug resistance and declining treatment efficacy in many cancers highlight the urgent need for new strategies with enhanced efficacy [7, 8], reduced side effects, and lower costs [9–11].

Recent developments in single-cell spatial transcriptomics have offered fresh insights into the inherent molecular mechanisms driving BLCA [12]. This technology facilitates precise mapping of the spatial distribution and gene expression profiles of different cell types within the tumor microenvironment (TME) [13, 14] and allows for the identification of the significant role of cuproptosis in BLCA [15]. Research has demonstrated that cuproptosis-related genes are highly expressed in tumor cells and are present at significant levels in immune cells, including macrophages and monocytes. This indicates a crucial role of cuproptosis in modulating immune responses within the TME, emphasizing its potential as a therapeutic target for BLCA [16].

In this context, metal–ligand and metal-polyphenol networks have attracted attention for their unique advantages in industrial and biomedical applications [17–19], particularly copper-based metal-polyphenol networks [20]. Copper generates reactive oxygen species (ROS) but also disrupts cellular redox homeostasis [21], leading to cell death [22, 23]. Vitexin (Vt), a natural flavonoid polyphenol, exhibits multiple biological activities, such as antioxidant, anti-inflammatory, and anticancer effects [24, 25]. Cu-VT nanoparticles (NPs) can be designed by integrating copper ions ($Cu2^{+}$) with VT to leverage the therapeutic benefits of both components [26].

Cu-VT NPs were designed and synthesized based on the data from single-cell spatial transcriptomics, to target the cuproptosis pathway in BLCA. Cu-VT NPs induce apoptosis by depleting glutathione (GSH) and generating ROS, while also modulating immune responses within the TME, significantly inhibiting tumor growth. The efficacy of Cu-VT NPs was evaluated and confirmed through in vitro as well as in vivo experiments. These nanoparticles could indeed directly induce cancer cell death and enhance antitumor immune responses through immunomodulation. This dual mechanism improves BLCA treatment efficacy as well as reduces side effects, showcasing their potential as a novel therapeutic approach for BLCA (Scheme 1). This innovative research approach offers an effective treatment option that may be crucial in future BLCA therapies.

2 Materials and methods

2.1 Acquisition and processing of single-cell-RNA sequencing (scRNA-seq) data

Three scRNA datasets were selected from the Gene Expression Omnibus (GEO) database: GSE130001, GSE146137, and GSE186520, each containing two samples of BLCA, for a total of six samples. Data were analyzed using R software (version 4.1.3) with the Seurat package. Criteria for quality control of cells included mitochondrial content of < 10%, UMI counts between 200 and 20,000, and gene counts of 200 to 6000. Data normalization, selection of highly variable genes ($n = 2000$), and data scaling (regressing out cell cycle effects with vars.to.regress = c ("S.Score," "G2M.Score")) were conducted, respectively, using the NormalizeData, FindVariableFeatures, and ScaleData functions from Seurat. Batch effect was corrected by employing Harmony. Dimensionality reduction techniques (UMAP, TSNE) and clustering algorithms (Louvain) were applied through Seurat. Differential gene expression across clusters or cell types was analyzed with the FindAllMarkers function, with parameters set to p-value < 0.05, log2FC > 0.25, and expression proportion > 0.1.

2.2 Cell annotation analysis

Cell annotation was performed employing markers for epithelial cells ("EPCAM," "KRT18," "KRT19," "CDH1"), fibroblasts ("DCN," "THY1," "COL1A1," "COL1A2"), endothelial cells ("PECAM1," "CLDN5," "FLT1," "RAMP2"), T cells ("CD3D," "CD3E," "CD3G," "TRAC"), NK cells ("NKG7," "GNLY," "NCAM1," "KLRD1"), B cells ("CD79A," "IGHM," "IGHG3," "IGHA2"), myeloid cells ("LYZ," "MARCO," "CD68," "FCGR3A"), and mast cells ("KIT," "MS4A2," "GATA2"). Based on these

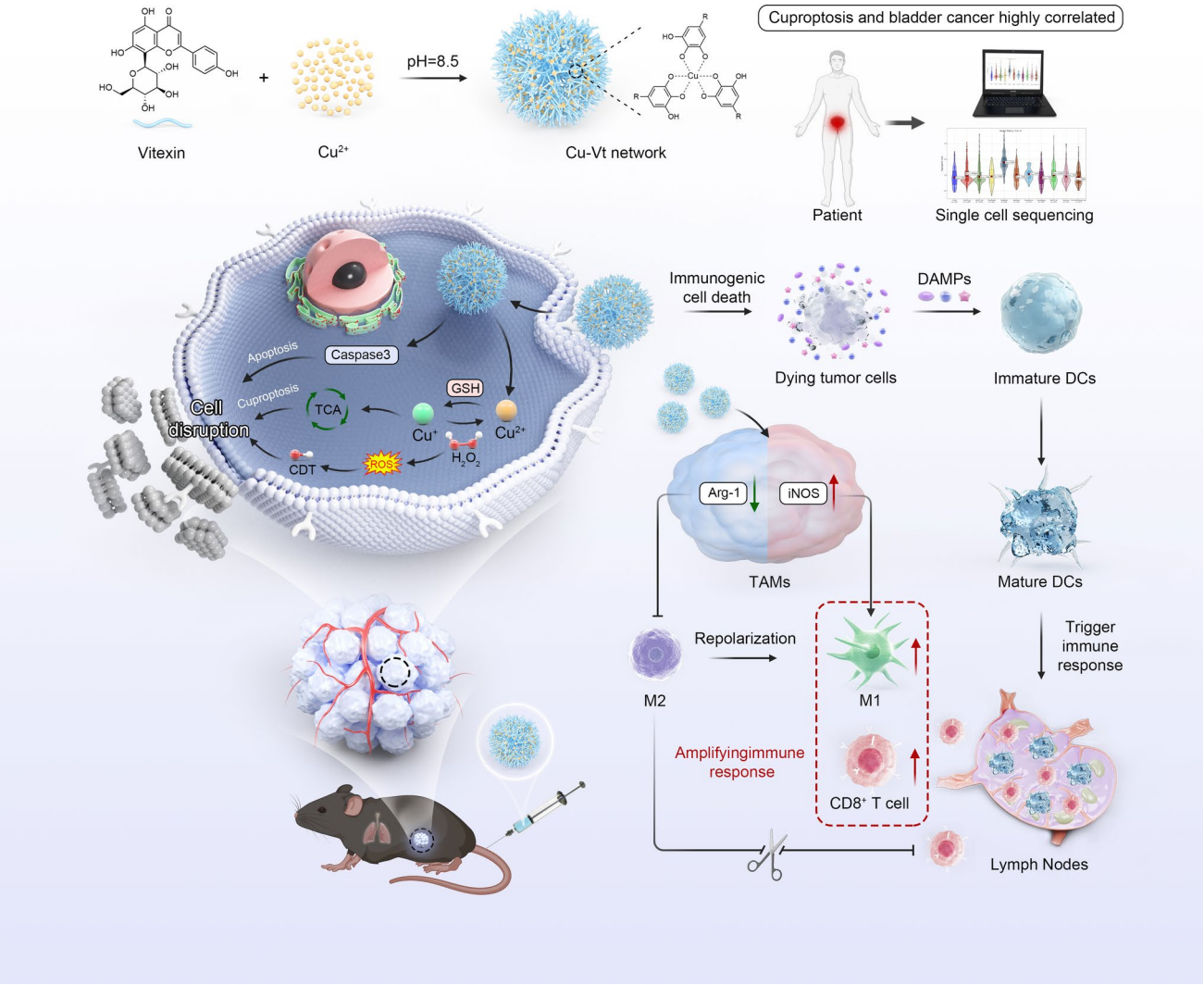

Scheme 1 Mechanism of action of Cu-VT NPs in bladder cancer (BLCA) Treatment. Single-cell sequencing results reveal a high correlation between cuproptosis and BLCA, leading to the preparation of Cu-VT NPs. These nanoparticles were synthesized by combining vitexin with $Cu2^{+}$ ions at pH 8.5, to form a Cu-VT network. This network induced cell disruption through apoptosis and cuproptosis, mediated by caspase-3 activation, glutathione (GSH) depletion, and ROS generation. Dying tumor cells release damage-associated molecular patterns (DAMPs), promoting the maturation of dendritic cells (DCs) and triggering an immune response. Tumor-associated macrophages (TAMs) shift from the M2 to the M1 phenotype, enhancing the rate of $CD8^{+}$ T cell activation and amplifying the immune response. The overall effect includes lung metastasis inhibition, highlighting the therapeutic potential of Cu-VT NPs in BLCA treatment

annotations, various visualizations, including t-distributed Stochastic Neighbor Embedding (t-SNE) plots and violin plots of cell markers, were created.

2.3 Spatial transcriptomics data processing

Spatial transcriptomics data were obtained from the GEO dataset GSE171351, which comprises four primary tumor samples. Data were analyzed using SpaceRanger software for quality control; this was followed by normalization, selection of highly variable genes, and data scaling using the SCTtransform algorithm. The Seurat package was employed for analysis and visualization. The conditional autoregression-based deconvolution (CARD) and CellTrek software were employed for deconvolution analysis, predicting cell types for each spot in the spatial transcriptomics data based on single-cell annotations. Cell types in the spatial transcriptomics data were visualized using the SpatialFeaturePlot function in Seurat. The cuproptosis scores were calculated using the AddModuleScore function in Seurat.

2.4 Materials and reagents

Copper(II) chloride (CuCl2) and Vt were procured from Aladdin (Shanghai, China). The reagents were purchased, including sodium hydroxide (NaOH, Macklin, Shanghai, China), polyethylene glycol (PEG, Sigma-Aldrich, Shanghai, China), Dulbecco's modified Eagle medium (DMEM), phosphate-buffered saline (PBS), trypsin–EDTA solution, Cell Counting Kit-8 (CCK-8), and DAPI were obtained from SparkJade (Shandong, China). Other reagents we purchased included fetal bovine serum (FBS, Wisent, Nanjing, China), Calcein-AM/PI and Annexin V-fluorescein isothiocyanate/propidium iodide (FITC/PI) (Bestbio, Shanghai, China), 2′,7′-dichlorofluorescin diacetate (DCFH-DA), and 5,5-dimethyl-1-pyrroline N-oxide (DMPO) from Biyotime (Shanghai, China). Antibodies for terminal-deoxynucleotidyl transferase-mediated nick end labeling (TUNEL), FDX1, dihydrolipoyl transacetylase (DLAT), CD206, Arg-1, CD86, and induced nitric oxide synthase (iNOS), as well as hydrogen peroxide (H_2O_2), reduced GSH, 3,3′,5,5′-tetramethylbenzidine (TMB), and 5,5′-dithiobis-(2-nitrobenzoic acid) (DTNB) were obtained from Macklin (Shanghai, China).

2.5 Production of Cu-VT NPs

Cu-VT NPs were synthesized by first dissolving $CuCl_2$ and Vt in distilled water at a molar ratio of 1:2. The solutions were then mixed thoroughly under high-speed stirring. The pH of the mixture was gradually adjusted to 8.5 by adding NaOH solution and monitored continuously to avoid overshooting. Subsequently, an appropriate amount of PEG was added to the mixture to stabilize and prevent aggregation of the nanoparticles. To ensure complete reaction and formation of Cu-VT NPs, the mixture was stirred at high speed for an extended period. The resulting nanoparticles were purified by centrifugation and washed with distilled water to remove unreacted materials and impurities. Finally, the purified Cu-VT NPs were stored in distilled water at 4 °C until further use.

The size and morphology of the Cu-VT NPs were analyzed through transmission electron microscopy (TEM). Nanomaterial elemental mapping was performed using energy-dispersive X-ray spectroscopy (EDS). X-ray photoelectron spectroscopy (XPS) was employed to analyze the surface composition and chemical states [27, 28].

2.6 Cell experiment

Cell viability assay MB49 and human umbilical vein endothelial cells (HUVEC) cells were cultured in appropriate media supplemented with 10% FBS and 1% penicillin–streptomycin. The cells were maintained at 37 °C in a humidified incubator with 5% CO_2 [29]. Cells were seeded in 96-well plates at a density of 5×10^3 cells per well. After 24 h, the cells were treated with different concentrations of Cu-VT NPs (0, 5, 10, 25, 50, 100 μg/mL) for 24 h. Next, cell viability was measured using the MTT assay. Briefly, after the treatment period, 20 μL of MTT solution (5 mg/mL) was added to each well and incubated for 4 h [30]. The medium was then removed, and the formazan crystals were dissolved using 150 μL of DMSO.

Fluorescence microscopy for live/dead cell staining Cells were stained using PI and Calcein-AM following treatment with Cu-VT NPs to differentiate live cells from dead cells. For this, Calcein-AM (2 μM) and PI (5 μg/mL) were added to the culture medium and incubated for 30 min at 37 °C. Stained cells were then washed with PBS and visualized under a fluorescence microscope [31].

Flow cytometry for apoptosis analysis After treatment, the cells were washed with cold PBS and resuspended at a concentration of 1×10^6 cells per mL. Subsequently, 5 μL of annexin V-FITC and 5 μL of PI were added to 100 μL of the cell suspension and incubated in the dark for 15 min at room temperature. After staining, 400 μL of 1 × binding buffer was added to each sample. Within 1 h, the samples were analyzed by flow cytometry. Data obtained with a BD FACSCalibur flow cytometer were analyzed using FlowJo software.

Glutathione levels MB49 cells were cultured in standard conditions and treated with Cu-VT NPs, CuCl2, or vitexin at specified concentrations for 24 h. Cells were stained with monochlorobimane, a fluorescent probe that specifically binds to GSH, and then visualized using a fluorescence microscope. GSH levels were measured in terms of the fluorescence intensity. Cells were harvested, washed, and stained with monochlorobimane. The GSH content was quantified by flow cytometry, and data were analyzed to determine the fluorescence intensity and the percentage of GSH-positive cells.

ROS generation In the post-treatment of cells, 2′,7′-dichlorodihydrofluorescein diacetate (DCFH-DA) was used as a fluorescent probe to determine the levels of ROS. Stained cells were visualized using a fluorescence microscope to determine ROS levels. Cells were collected, washed, and stained with DCFH-DA. ROS levels and the percentage of DCF-positive cells were quantified using flow cytometry [32].

Western blot analysis MB49 cells were treated with Cu-VT NPs, CuCl2, and vitexin for 24 h. The cells were lysed in RIPA buffer containing protease and phosphatase inhibitors. Protein samples were separated by sodium dodecyl sulfate–polyacrylamide gel electrophoresis (SDS-PAGE)

and transferred onto PVDF membranes. The proteins were transferred onto polyvinylidene fluoride membranes after SDS-PAGE and blocked with 5% non-fat milk in TBST. Then, antibodies against dihydrolipoamide S-acetyltransferase (DLAT), Lipoic Acid Synthetase (LIAS), Ferredoxin 1 (FDX1), and β-Actin were added and incubated overnight at 4 °C. Membranes were then incubated with horseradish peroxidase-conjugated secondary antibodies and developed using enhanced chemiluminescence detection reagents. Band intensities were quantified using ImageJ software.

Quantitative real-time-polymerase chain reaction (qRT-PCR) analysis Total RNA was extracted from treated MB49 cells using TRIzol reagent. RNA was reverse-transcribed into cDNA using a cDNA synthesis kit, and qRT-PCR was performed employing SYBR Green Master Mix on a real-time PCR system. Primers specific for DLAT, LIAS, FDX1, and dihydrolipoamide dehydrogenase (DLD) were used. To calculate the relative gene expression, the 2^ − ΔΔCt method was used, normalized to GAPDH. The primer sequences were as follows:

DLAT: Forward: 5′-CGGACTACCTTCCAGCCTAC-3′, Reverse: 5′-AGGACACAGTGCCAGGATAG-3′
LIAS: Forward: 5′-GACACGATGCAGAACATCGA-3′, Reverse: 5′-GACTGAGGTGAGGATGAGGA-3′
FDX1: Forward: 5′-TGTGGTGGAGATGTTCTGGA-3′, Reverse: 5′-CAGTGGTGTTGTGGAAGGAG-3′
DLD: Forward: 5′-CGTTGTGGAAAGGACTCCTG-3′, Reverse: 5′-GGTGAGGAAGGTTGGTGACT-3′
GAPDH: Forward: 5′-GACATGCCGCCTGGAGAAAC-3′, Reverse: 5′-AGCCCAGGATGCCCTTTAGT-3′

Transwell migration assay 5×10^4 MB49 cells were seeded in the upper chamber of transwell inserts with serum-free medium. The lower chamber harbored medium with 10% FBS as a chemoattractant. To the lower surface of the insert, 4% paraformaldehyde solution was applied, and after 24 h, the migrated cells were stained using crystal violet. Migrated cells were visualized using a light microscope, and cell counts were performed using ImageJ software [33].

Wound healing assay MB49 cells were seeded in 6-well plates and grown to confluence. A scratch was made on the cell layer using a pipette tip, and cells were treated with Cu-VT NPs, $CuCl_2$, and Vt. Wound closure was monitored at 0 and 24 h. Images of the wound area were acquired using a phase-contrast microscope and quantified using ImageJ software to calculate the healing rate [34].

2.7 Animal experiment

Animal model and treatment MB49 BLCA cells were injected subcutaneously into female C57BL/6 nude mice (4–6 weeks old) to establish the tumor model. Once tumors reached an average volume of 100 mm3, mice were randomly categorized into four groups: $c^{ontrol,\ CuCl}{}_2$, Vitexin (VT), and Cu-VT NPs. Treatments were administered through tail vein injection every 3 days for 15 days. Every 2 days, tumor volumes were measured with calipers and calculated using the formula: volume = 1/2 × length × width2. After the treatment period ended, tumors were excised, photographed, and weighed. Body weights were recorded every 2 days any potential systemic toxicity of the treatments was monitored.

Histological and immunohistochemical analysis Excised tumors were fixed in 10% formalin, embedded in paraffin, and sectioned. Apoptosis and proliferation in tumor sections were assessed by staining with antibodies against caspase-3 and Ki67, respectively. To visualize ROS generation, tumor sections were also stained with DAPI and ROS-sensitive dyes.

Immunohistochemistry (IHC) The excised tumor sample was fixed in 10% formalin, embedded in paraffin, and sectioned (thickness 3–5 μm). The sections were deparaffinized and rehydrated, and antigen retrieval was performed. Primary antibodies against TUNEL, FDX1, and DLAT were added, followed by the addition of appropriate secondary antibodies, and incubated. The sections were visualized using the DAB substrate and counterstained with hematoxylin. Stained sections were visualized using a light microscope, and the levels of expression were quantified using ImageJ software.

Immunofluorescence (IF) Tumor sections were stained with primary antibodies against CD206/Arg-1 and CD86/iNOS and then incubated with fluorescence-conjugated secondary antibodies. Nuclei were counterstained with DAPI. Sections were finally imaged using a fluorescence microscope, and the expression levels were quantified.

Flow cytometry Tumor tissues were macerated and digested with collagenase to obtain single-cell suspensions. Cells were stained with antibodies against CD3, CD8, CD206, and CD86 conjugated with fluorophore. Stained cells were examined using a flow cytometer, and data were processed with FlowJo software to quantify the proportions of $CD8^+$ T cells and tumor-associated macrophage (TAM) subsets (M1 and M2 phenotypes) [35].

2.8 Biochemical analysis

At the end of the treatment period, blood samples from mice were collected via cardiac puncture. Serum was isolated and analyzed for total bilirubin (TBIL), alanine aminotransferase (ALT), aspartate aminotransferase (AST), blood urea nitrogen (BUN), creatinine (CR), and glucose (GLU) content using an automatic biochemical analyzer. Whole blood was examined using a hematology analyzer to determine red blood cell count (RBC), mean corpuscular hemoglobin (MCH), white blood cell count (WBC), mean corpuscular hemoglobin concentration (MCHC), mean corpuscular volume (MCV), and platelet count (PLT). After euthanasia, major organs, including the lung, heart, liver, kidney, and spleen, were harvested. These samples were preserved in 10% formalin, then treated, and embedded in paraffin. The paraffin-encased samples were sliced into 5-μm sections and stained with hematoxylin and eosin (H&E) for histopathological analysis. Stained sections were examined under a light microscope, and representative images were acquired for analysis [35].

3 Results and discussion

3.1 Single-cell spatial transcriptomics reveals the correlation of cuproptosis in bladder cancer

The single-cell transcriptomics analysis offers comprehensive insights into the correlation between cuproptosis and BLCA, as illustrated by the datasets GSE130001, GSE146137, and GSE186520 (Supplementary Fig. 1) [36]. The t-SNE clustering plots (left panels) illustrate the spatial distribution of various cell types within BLCA tissues, including tumor cells, immune cells, endothelial cells, and fibroblasts. The heatmaps in the middle present the expression levels of cuproptosis-related genes across these cell types. Violin plots (right panels) show the quantitative expression levels of genes involved in cuproptosis in different cell types, revealing significantly higher expression in tumor cells relative to other cell types (Kruskal–Wallis test, $P < 2.2e-16$). The high expression level of cuproptosis-related genes in tumor cells suggests a critical role of cuproptosis in BLCA pathogenesis. The expression of these genes in immune cells, including macrophages and monocytes, indicates a potential involvement of cuproptosis in regulating the immune response within the TME.

Further spatial transcriptomics analysis illustrates the localization of various cell types within the TME and the corresponding expression of cuproptosis-related genes (Supplementary Fig. 2). The left panels show the spatial distribution of cell types, and the middle panels present the overlap of cuproptosis gene expression. Violin plots on the right present the quantification of these expression levels, revealing significant differences among different cell types (Kruskal–Wallis test, $P < 2.2e-16$). These results further emphasize the significant role of cuproptosis in tumor cells and highlight its potential impact on immune cell function within the TME. The high expression of cuproptosis-associated genes in both tumor and immune cells highlights their key roles in tumor biology and immune regulation, providing valuable insights into the molecular mechanisms underpinning BLCA progression.

This section provides an in-depth spatial transcriptomics analysis of BLCA, highlighting a significant correlation between cuproptosis-related gene expression and tumor cell pathology. The data, visualized through t-SNE clustering, heatmaps, and violin plots, reveal a higher expression of cuproptosis-associated genes in tumor cells compared to other cell types, emphasizing cuproptosis's critical role in BLCA pathogenesis [37]. Additionally, cuproptosis gene expression in immune cells suggests a regulatory function within the TME, with CARD software further validating cell-type distribution and enrichment, particularly of epithelial cells, across slides. These findings elucidate the molecular underpinnings of BLCA progression and immune interaction [38].

3.2 Synthesis and characterization of Cu-VT NPs

The Cu-VT NPs were synthesized using a straightforward metal-polyphenol coordination method. The size and morphology of the Cu-VT NPs were analyzed through transmission electron microscopy (TEM) (Fig. 1A–C). Statistical analysis of the TEM images shows that the average size of Cu-VT NPs was 2–3 nm (Fig. 1B), indicating a well-controlled synthesis process with uniform particle size. For applications in biomedicine, the high monodispersity and narrow size distribution of Cu-VT NPs are crucial. Nanomaterial elemental mapping was performed using energy-dispersive X-ray spectroscopy (EDS) to investigate the distribution of carbon (C), nitrogen (N), oxygen (O), and copper (Cu). This analysis aimed to evaluate the compositional uniformity and spatial distribution of these elements within the sample. Figure 1D–E present the results of EDS mapping, where each element is depicted in a distinct color, with red indicating carbon, green indicating nitrogen, blue indicating oxygen, and yellow indicating copper. The mappings demonstrate a uniform distribution of C, N, O, and Cu throughout the material, indicating these elements had a consistent composition. Figure 1F shows the HAADF-STEM image, highlighting the high-contrast atomic structure. The brighter regions represent the heavier element (Cu), while the darker regions represent the lighter elements (C, N, and O). X-ray photoelectron spectroscopy (XPS) was employed to analyze the

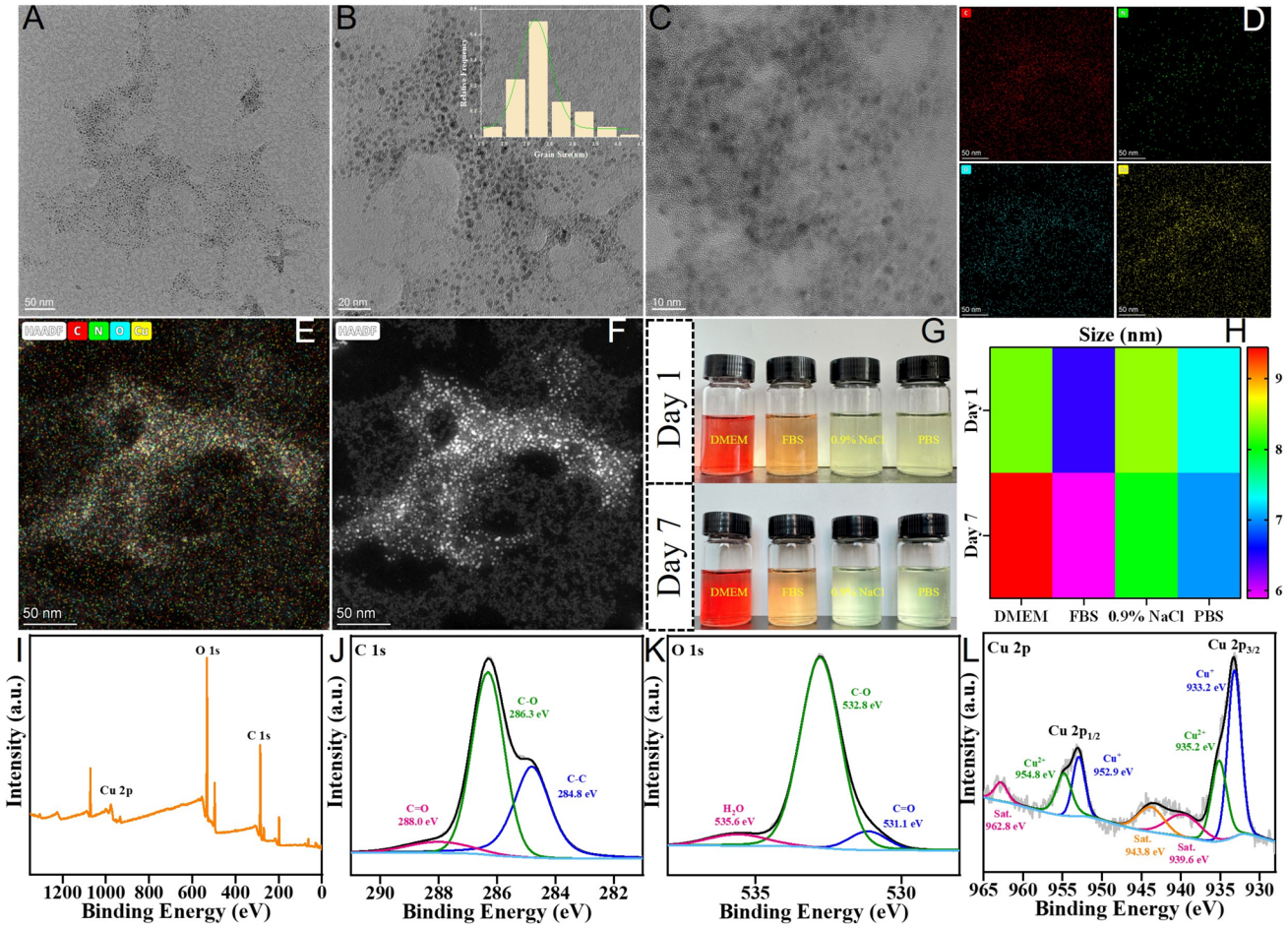

Fig. 1 Characterization of Cu-VT NPs. **A**–**C** Transmission electron microscopy images of Cu-VT NPs at different scales. **D**, **E** Elemental mapping of Cu-VT NPs using energy dispersive X-ray spectroscopy, with each element shown in a different color: carbon (red), nitrogen (green), oxygen (blue), and copper (yellow). **F** High-angle annular Dark Field Scanning Transmission Electron Microscopy (HAADF-STEM) image of Cu-VT NPs. **G** An image of nanomaterial suspensions in phosphate-buffered saline, fetal bovine serum, 0.9% NaCl, and Dulbecco's Modified Eagles Medium after 1 week. **H** Particle size distribution of the nanomaterial in the four media pre- and post-1 week of incubation, measured by dynamic light scattering. **I** X-ray photoelectron spectroscopy (XPS) survey spectrum of Cu-VT nanoparticles showing the presence of C, O, and Cu. **J**–**K** High-resolution XPS spectra of C 1 s and O 1 s for Cu-VT NPs. **L** High-resolution XPS spectrum of Cu 2p for Cu-VT NPs

surface composition and chemical states of the Cu-VT nanoparticles. Figure 1G showed that Cu-VT was dispersed in DMEM, FBS, 0.9% NaCl, and PBS, and there was no obvious precipitation or aggregation after 1 day and 7 days, indicating that Cu-VT had good stability under various physiological conditions. The thermal map shows the variation of particle size distribution of Cu-VT in different media. The particle size remained stable after 1 day and 7 days without significant change whether in DMEM, FBS, 0.9% NaCl, or PBS, further verifying its excellent size stability (Fig. 1H). Figure 1I presents the survey spectrum, indicating the presence of carbon (C), oxygen (O), and copper (Cu) in the sample. Figure 1J–K present the high-resolution XPS spectra for C 1 s, O 1 s, and Cu 2p. The C 1 s spectrum demonstrates peaks corresponding to various C-containing functional groups, indicating the presence of graphitic as well as oxidized carbon species. The O 1 s spectrum shows peaks characteristic of oxygen species bonded to Cu and C, confirming the formation of Cu–O and C-O bonds. The Cu 2p spectrum, as shown in Fig. 1L, presents two main peaks corresponding to Cu 2p 3/2 and Cu 2p 1/2, along with their respective satellite peaks. These peaks indicate the presence of Cu^{2+} in the Cu-VT NPs, suggesting that the copper ions within the nanomaterial had successfully coordinated.

The Cu-VT NPs were synthesized using a metal-polyphenol coordination method, resulting in a uniform particle size of 2–3 nm as shown by TEM analysis. Elemental mapping and XPS characterization confirmed the homogeneous distribution of C, N, O, and Cu, with Cu2 + ions effectively

coordinated within the nanomaterial. These structural and compositional features underscore the potential of Cu-VT NPs for biomedical applications [39].

3.3 The POD enzyme activity of Cu-VT NPs

According to previous reports on the catalytic performance of Cu-based nanozymes, Cu-VT NPs were hypothesized to possess GSH depletion activity and POD-like enzyme activity. Thus, relevant tests were carried out to evaluate their performance. High levels of GSH within tumor cells can neutralize excess ROS, thereby reducing cell damage. Hence, the depletion of GSH within tumor cells can amplify oxidative stress, leading to apoptosis, a catalytic activity referred to as glutathione peroxidase (GSH-Px). Thus, the GSH depletion capability of Cu-VT NPs was examined. As shown in Fig. 2A, the GSH depletion capability of Cu-VT NPs increased with the concentration. The peroxidase (POD) enzyme activity of Cu-based nanozymes is crucial in the treatment of tumor microenvironments (TMEs). To this end, the POD enzyme activity of Cu-VT NPs was evaluated. Colorimetric assays using TMB and POD were conducted, as shown in Fig. 2B and C, demonstrating that Cu-VT exhibited significant POD enzyme activity. Furthermore, the POD

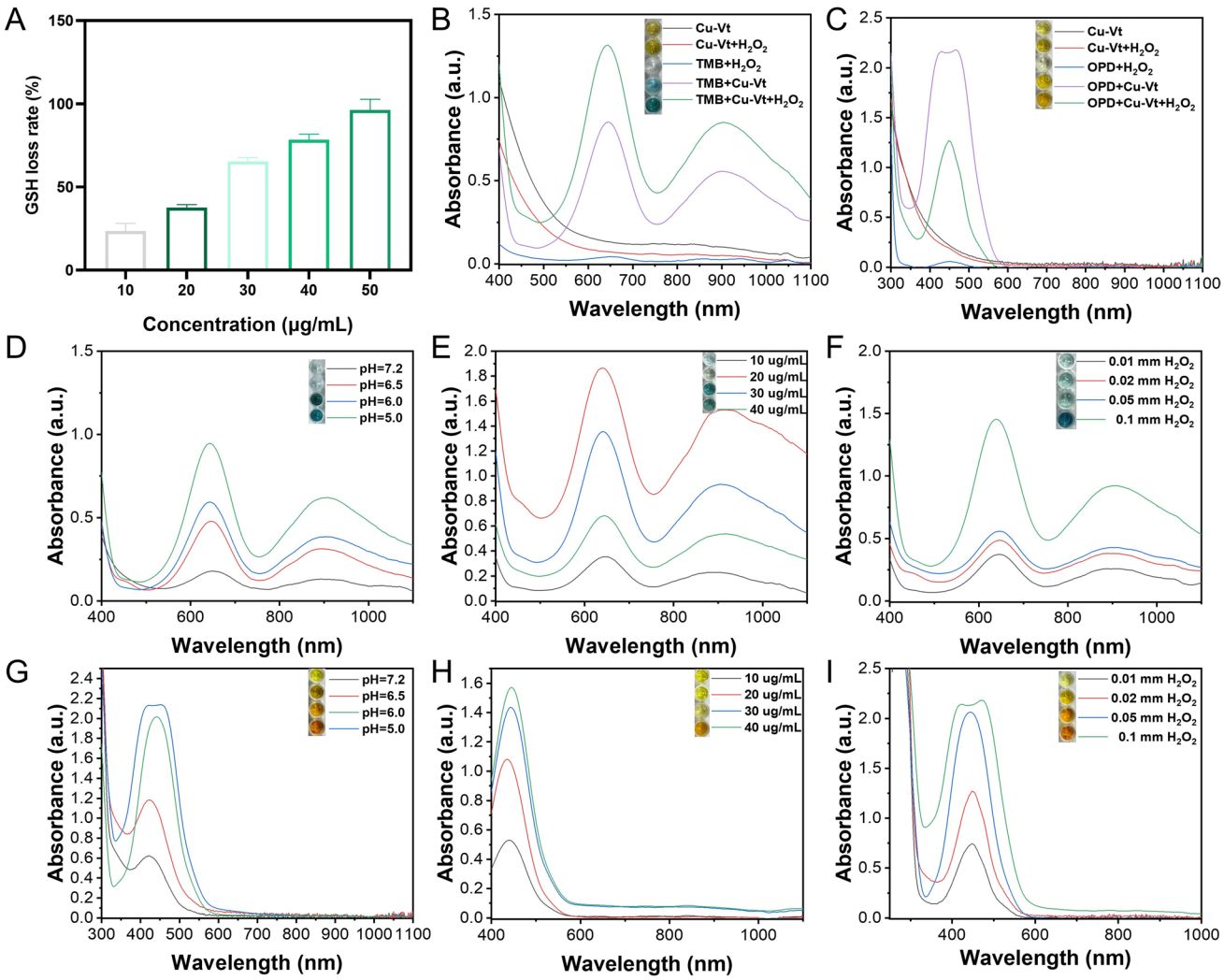

Fig. 2 Glutathione (GSH) depletion and POD-like activity of Cu-VT NPs. **A** The rate of GSH loss at varying Cu-VT NP concentrations, showing concentration-dependent GSH depletion. **B** TMB (3,3′,5,5′-tetramethylbenzidine) oxidation by Cu-VT NPs with/without H2O2, indicating peroxidase (POD)-like activity. **C** POD oxidation by Cu-VT NPs with/without H2O2, confirming POD-like activity. **D** TMB oxidation at different pH values, with enhanced activity under acidic conditions. **E** TMB oxidation at varying Cu-VT NPs concentrations, showing concentration-dependent activity. **F** TMB oxidation at different H_2O_2 concentrations, showing dependence on H_2O_2. **G** OPD oxidation at different pH values, showing enhanced activity under acidic conditions. **H** OPD oxidation at varying Cu-VT NPs concentrations, showing concentration-dependent activity. **I** OPD oxidation at different H_2O_2 concentrations, showing H_2O_2 dependence

enzyme activity of Cu-VT increased with decreasing pH, as illustrated in Fig. 2D and G, indicating enhanced performance in the mildly acidic TMEs. Additionally, the POD enzyme activity increased with the concentration of Cu-VT NPs, Fig. 2E and H. Moreover, at a constant concentration of Cu-VT NPs, the absorbance of the characteristic POD peak increased with the concentration of H_2O_2 (Fig. 2F and I). These results collectively indicate excellent GSH depletion capability and POD enzyme activity of Cu-VT NPs, highlighting their potential application in TMEs.

The Cu-VT NPs demonstrated both GSH depletion activity and POD-like enzyme activity, essential for increasing oxidative stress in tumor microenvironments (TMEs) [40]. Concentration-dependent GSH depletion and enhanced POD activity, especially under acidic conditions and with increased H_2O_2, underscore their therapeutic potential for modulating TMEs [41].

3.4 Biocompatibility and antitumor efficiency of the Cu-VT NPs in vitro

The cytotoxicity of Cu-VT NPs was evaluated on MB49 BLCA cells and HUVEC endothelial cells. In MB49 cells, there was a dose-dependent decrease in cell viability with increasing concentrations of Cu-VT NPs, demonstrating significant cytotoxicity at higher concentrations (Fig. 3A). In contrast, there was no significant change in the viability of HUVEC cells over the same concentration range, indicating a selective toxicity of Cu-VT NPs towards cancer cells (Fig. 3B). The superior efficacy of Cu-VT NPs over other treatments was confirmed by further comparison among different treatment groups in MB49 cells (Fig. 3C).

Fluorescence microscopy and quantitative analysis revealed a substantial increase in dead cells in the Cu-VT treatment group (Fig. 3D and E). Calcein-AM staining, which stains viable cells in green, and PI staining, which stains dead cells in red, showed that the number of red-stained cells increased notably in the Cu-VT group. This observation was further supported by quantitative data, which indicates that Cu-VT NPs effectively induce cell death in MB49 cells. These findings were further corroborated by flow cytometry analysis (Fig. 3F). Annexin V-FITC/PI double staining demonstrated a significant increase in both early and late apoptotic cells in the Cu-VT treatment group, and the cells in the late apoptosis stage (Q2) reached 38.7%, markedly higher than in the control, $CuCl_2$, and VT groups. These results suggest anticancer effects of Cu-VT NPs primarily through the induction of apoptosis. In summary, Cu-VT NPs exhibit potent and selective cytotoxicity against MB49 BLCA cells, primarily through the induction of apoptosis, while sparing normal HUVEC cells.

The impact of Cu-VT NPs on intracellular GSH levels and ROS generation in MB49 cells was evaluated. Fluorescence microscopy and flow cytometry revealed a significant decline in GSH levels in Cu-VT treated cells compared to that in the control, $CuCl_2$, and VT groups, with a notable reduction in fluorescence intensity (Fig. 4A–C). Concurrently, ROS generation increased markedly in Cu-VT-treated cells, as evidenced by DCFH-DA staining and flow cytometry (Fig. 4E and F). The Cu-VT treated group showed intense green fluorescence, suggesting elevated ROS levels, and flow cytometry confirmed a high percentage of DCF-positive cells (81.9%) compared to the number of cells in the control (1.88%), $CuCl_2$ (11.5%), and vitexin (3.22%) groups. Quantitative analysis further corroborated these findings, demonstrating a significant increase in DCF fluorescence intensity in the Cu-VT treated group (Fig. 4D). These results suggest that Cu-VT NPs induce oxidative stress through the depletion of GSH and enhancing ROS production. This oxidative stress likely underlies the cytotoxic effects of Cu-VT NPs.

Cu-VT NPs exhibit selective cytotoxicity against MB49 BLCA cells by inducing apoptosis, while sparing normal HUVEC cells. The nanoparticles significantly reduced intracellular GSH levels and increased ROS generation in MB49 cells, as confirmed by fluorescence microscopy and flow cytometry, suggesting that oxidative stress plays a central role in their cytotoxic mechanism. These findings highlight the potential of Cu-VT NPs for targeted cancer therapy [42].

3.5 In vitro cuproptosis evaluation

The effects of Cu-VT NPs on cuproptosis pathways and MB49 cell migration were analyzed. Western blotting revealed that Cu-VT treatment significantly decreased the levels of DLAT, LIAS, and FDX1 proteins compared to those in the control, $CuCl_2$, and VT groups, with β-actin as a loading control (Fig. 5A). Quantitative assessment of the band intensities confirmed these findings, showing effective inhibition of the cuproptosis pathway (Fig. 5B). QRT-PCR analysis showed a significant downregulation of DLAT, LIAS, FDX1, and DLD mRNA levels, consistent with the results of protein analyses (Fig. 5C). The transwell migration and wound healing assays demonstrated that Cu-VT NPs markedly inhibited MB49 cell migration (Fig. 5E and F), as evidenced by a decline in cell migration (Fig. 5D) and wound closure rates (Fig. 5G), and Cu-VT treated cells showed a significantly lower cell activity. These findings suggest that Cu-VT NPs disrupt cellular Cu homeostasis by downregulating key enzymes and genes of the cuproptosis pathway and significantly impeding MB49 cell migration, highlighting their potential as therapeutic agents against BLCA through the modulation of Cu-induced cell death mechanisms and inhibition of cancer cell migration.

Cu-VT NPs effectively disrupt the cuproptosis pathway in MB49 cells by downregulating DLAT, LIAS, FDX1, and

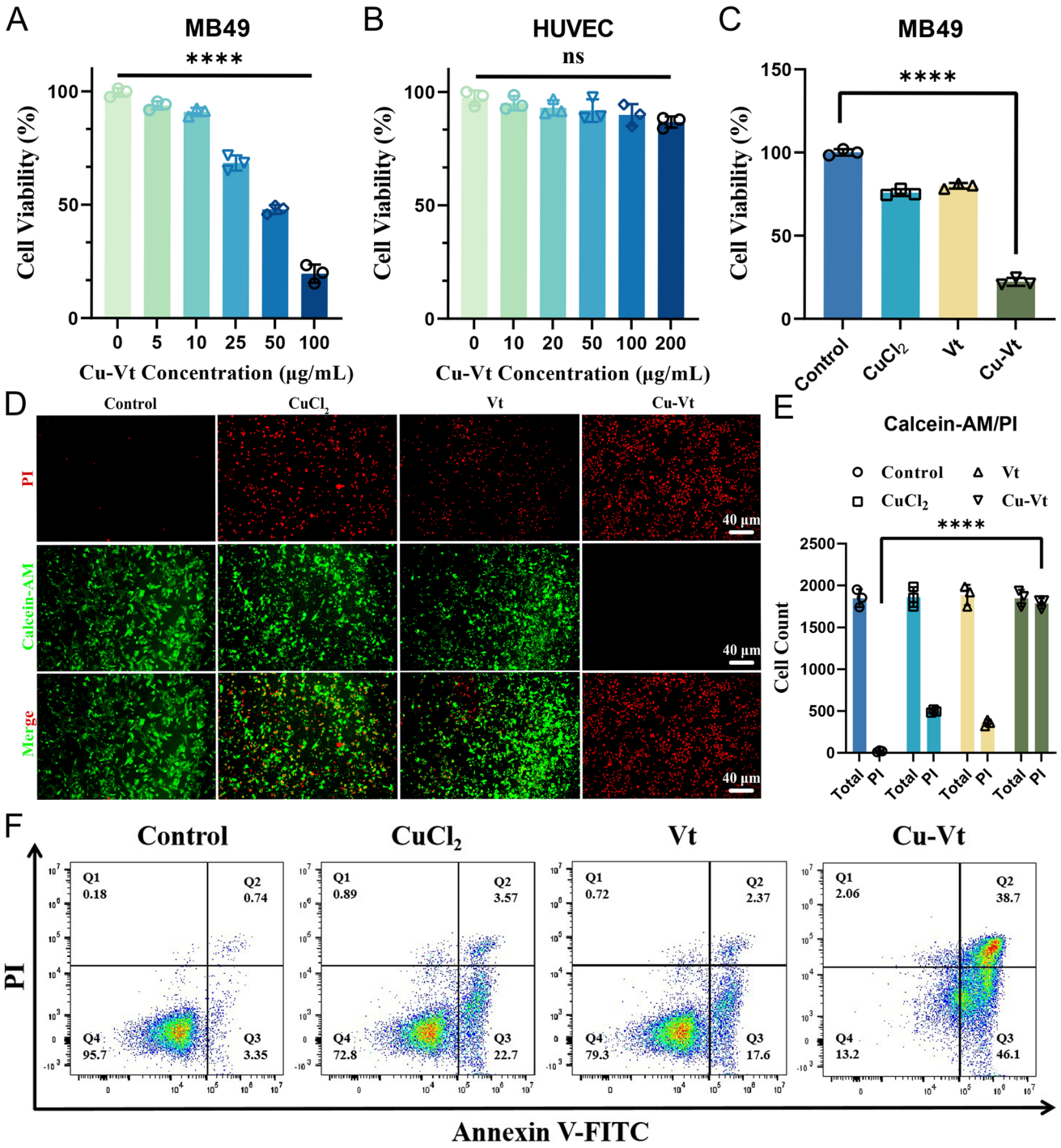

Fig. 3 Evaluation of cell viability and cytotoxicity of Cu-VT NPs. **A** Viability of human umbilical vein endothelial cells (HUVECs) at varying concentrations of Cu-VT NPs. **B** Viability of MB49 cells at different Cu-VT NP concentrations. **C** Comparison of MB49 cell viability after treatment with control, $CuCl_2$, VT, and Cu-VT NPs. **D** Live/dead staining (Calcein-AM/PI) of MB49 cells post-treatment with control, $CuCl_2$, VT, and Cu-VT NPs, shows a higher number of dead cells (red) in the Cu-VT NPs group compared to live cells (green). **E** Quantification of live/dead stained cells. **F** Flow cytometry analysis of apoptosis in MB49 cells using Annexin V-FITC/propidium iodide staining. Data are shown as mean ± standard deviation. Statistical significance is indicated by $^{****}P < 0.0001$. Scale bars represent 40 μm

DLD at both protein and mRNA levels [43]. Additionally, they inhibit MB49 cell migration, as shown by transwell and wound healing assays. These findings underscore the therapeutic potential of Cu-VT NPs in targeting BLCA by modulating cuproptosis-related pathways and restricting cancer cell motility [44].

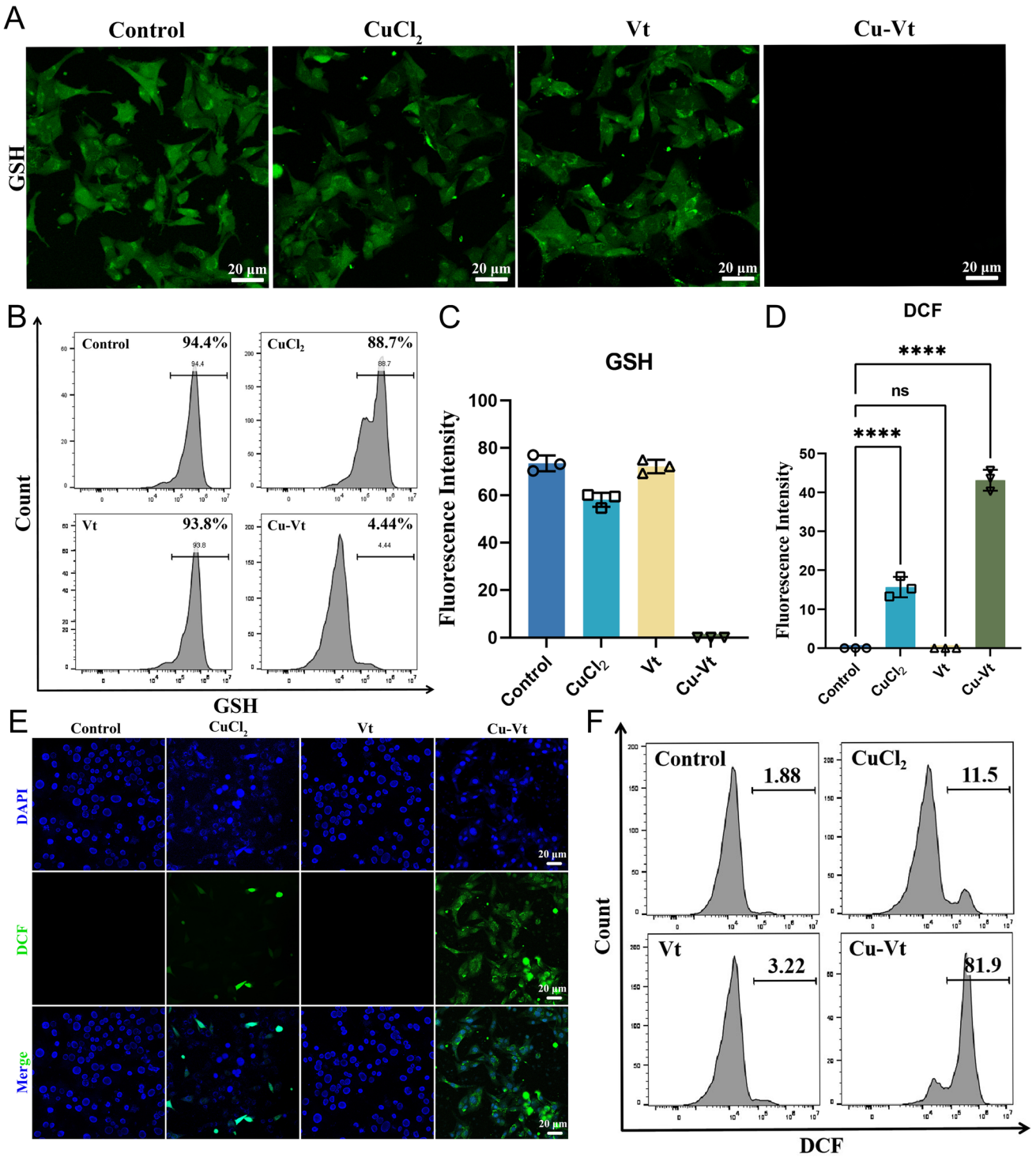

Fig. 4 Effects of Cu-VT NPs on intracellular glutathione (GSH) levels and the production of reactive oxygen species (ROS) in MB49 cells. **A** Fluorescence microscopy images showing GSH levels. **B** Flow cytometry analysis of GSH content. **C** Quantification of GSH through fluorescence intensity. **D** Quantification of ROS through fluorescence intensity. **E** Fluorescence microscopy images of ROS levels using DCFH-DA staining. **F** Flow cytometry analysis of ROS generation. Results are expressed as mean ± standard deviation. Statistical significance is marked by $*P<0.05$, $**P<0.01$, $***P<0.001$, and $****P<0.0001$. Scale bars denote 20 μm

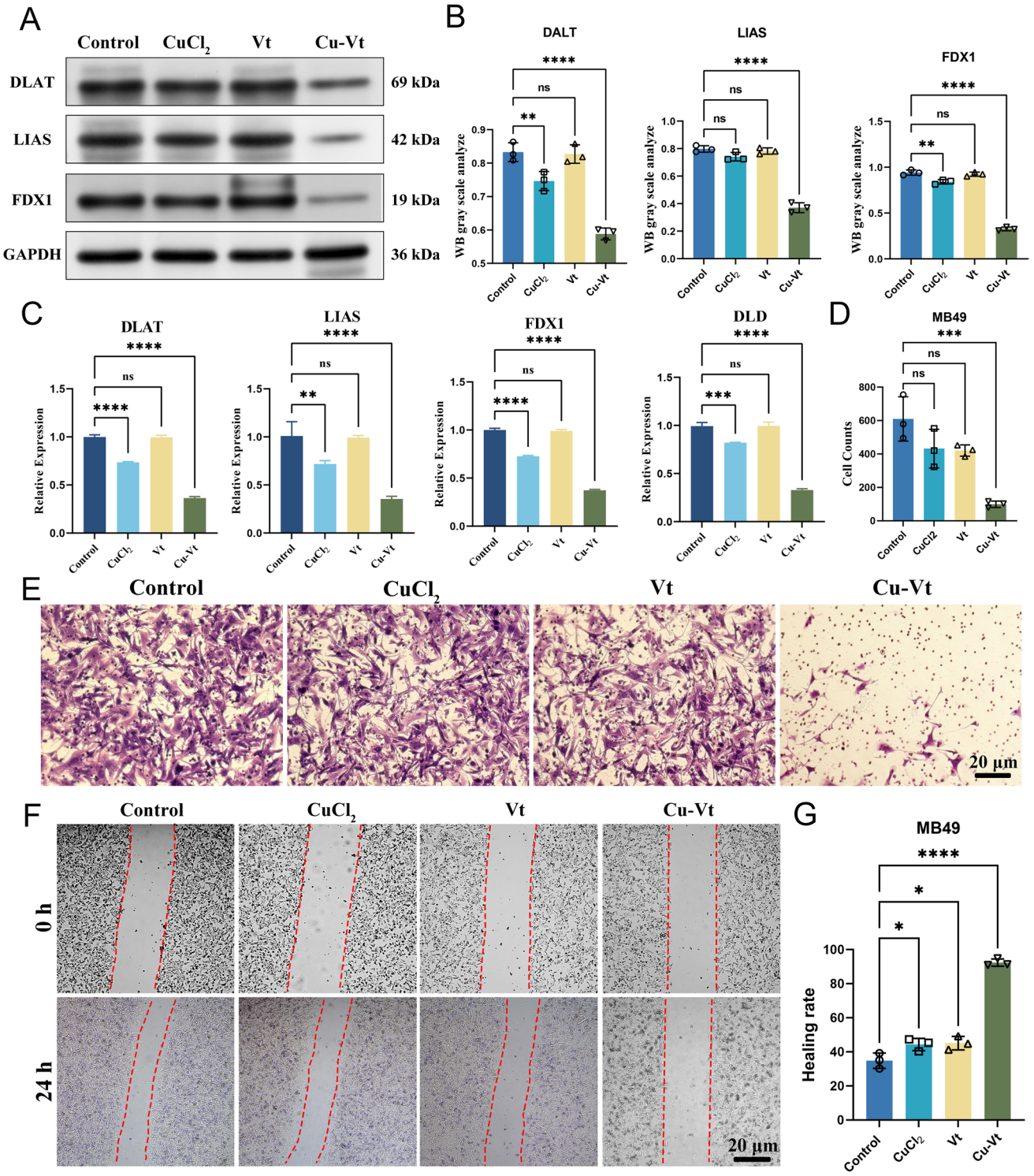

Fig. 5 Impact of Cu-VT NPs on the cuproptosis pathway and cell migration in MB49 cells. **A** Western blot analysis showing the levels of DLAT, LIAS, and FDX1 proteins, with β-Actin as a loading control. **B** Quantitative measurement of protein band intensities. **C** Relative mRNA expression levels of DLAT, LIAS, FDX1, and DLD as determined by quantitative real-time-polymerase chain reaction. **D** Cell counts of MB49 cells. **E** Representative images of transwell migration assay. **F** Wound healing assay images at 0 and 24 h. **G** Measurement of wound healing rates. Results are shown as mean ± standard deviation. Statistical significance is denoted by $*P<0.05$, $**P<0.01$, $***P<0.001$, and $****P<0.0001$. Scale bars represent 20 μm

3.6 Transcriptomic analysis of MB49 cells treated with Cu-VT NPs

A heatmap of differentially expressed genes (DEGs) between control and Cu-VT-treated MB49 cells is shown in Fig. 6A, indicating significant changes in gene expression profiles upon treatment. A volcano plot highlighting upregulated (red) and downregulated (blue) genes is presented in Fig. 6B; key genes related to the cuproptosis pathway, such as Atf3 and Mt1, were upregulated; those associated with cellular stress response, Lias, and Fdx1 were downregulated. Figure 6C presents the Gene Set Enrichment Analysis results, with the top panel illustrating enrichment scores for downregulated pathways and the bottom panel presenting pathways upregulated in Cu-VT treated cells. The analysis demonstrated significant enrichment in pathways associated with cell differentiation and immune response regulation, including mononuclear cell differentiation (GOBP_MONONUCLEAR_CELL_DIFFERENTIATION) and response to endogenous stimulus (GOBP_RESPONSE_TO_ENDOGENOUS_STIMULUS) in downregulated genes, and chromatin assembly or disassembly (GOBP_CHROMATIN_ASSEMBLY_OR_DISASSEMBLY) and chromatin remodeling (GOBP_CHROMATIN_REMODELING) in upregulated genes.

The Gene Ontology (GO) and Kyoto Encyclopedia of Genes and Genomes (KEGG) pathway enrichment analyses for downregulated (Fig. 6D) and upregulated (Fig. 6E) genes, respectively, were performed. As shown in Fig. 6D, downregulated genes exhibit significant enrichment in pathways related to metabolic processes and cellular component organization, such as DNA-dependent transcription repressor activity (GO_DNA_DEPENDENT_TRANSCRIPTION_REPRESSOR_ACTIVITY) and transcription coregulator activity (GO_TRANSCRIPTION_COREGULATOR_ACTIVITY). KEGG pathway analysis further showed key downregulated pathways that included EGFR tyrosine kinase inhibitor resistance and ErbB signaling pathway.

The upregulated genes were significantly enriched in pathways related to immune response and cell death processes (Fig. 6E), such as response to oxidative stress (GO_RESPONSE_TO_OXIDATIVE_STRESS) and growth factor activity (GO_GROWTH_FACTOR_ACTIVITY). KEGG pathway analysis revealed key upregulated pathways, including those involved in systemic lupus erythematosus and neutrophil extracellular trap formation.

These transcriptomic outcomes revealed the molecular basis of the effects of Cu-VT NPs in inducing apoptosis and cuproptosis, disrupting cellular homeostasis, and enhancing immune response. The marked downregulation of metabolic pathways and upregulation of immune-related pathways

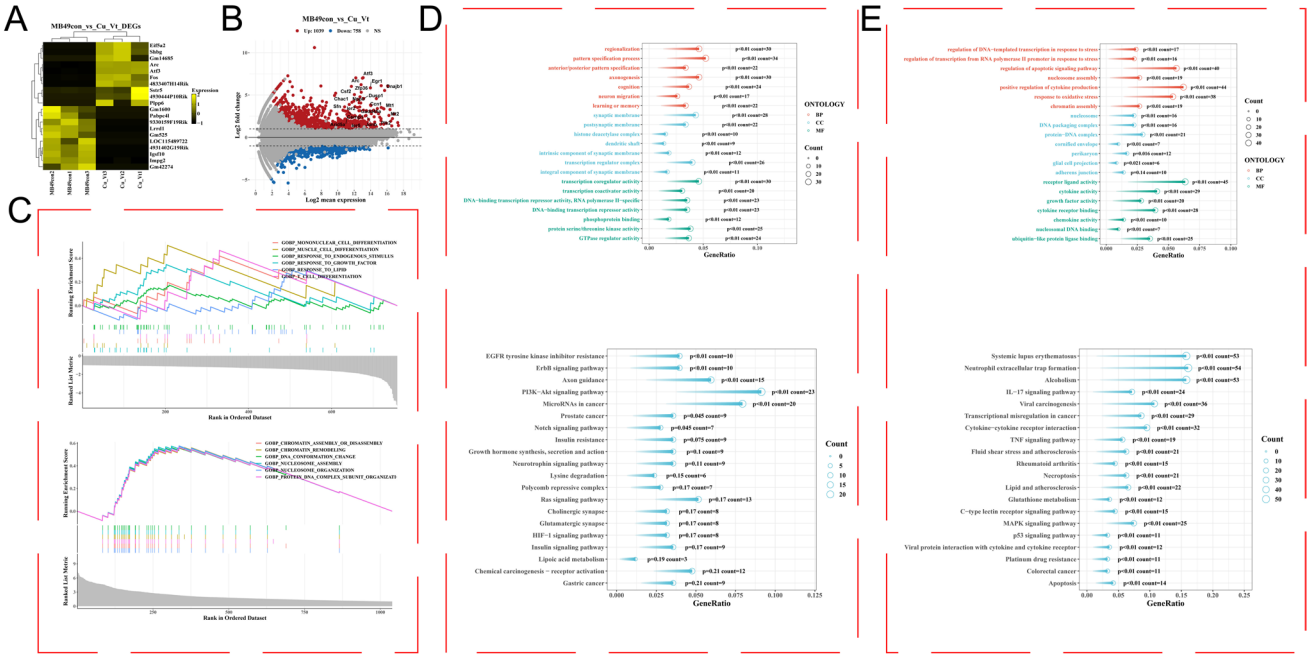

Fig. 6 Transcriptomic analysis of MB49 cells following Cu-VT NP treatment. **A** Heatmap displaying differentially expressed genes (DEGs) between control and Cu-VT treated cells. **B** Volcano plot presenting upregulated (red) and downregulated (blue) genes. **C** Gene Set Enrichment Analysis showcasing downregulated (top) and upregulated (bottom) pathways. **D** Gene Ontology (GO) and Kyoto Encyclopedia of Genes and Genomes (KEGG) pathway enrichment analyses for downregulated genes. **E** GO and KEGG pathway enrichment analyses for upregulated genes

align with the proposed mechanism where Cu-VT NPs induce cell death through caspase-3 activation, GSH depletion, and ROS generation, leading to the subsequent release of DAMPs and subsequent immune activation. This dual action, combining direct cytotoxic effects with the stimulation of antitumor immunity, highlights the therapeutic potential of Cu-VT NPs in BLCA treatment.

3.7 In vivo therapeutic efficacy of Cu-VT NPs

The in vivo efficacy of Cu-VT NPs in a mouse model of BLCA was evaluated. The experimental design depicted in Fig. 7A shows that mice were injected via the tail vein with the different treatments and sacrificed on day 15 for further analysis. Tumor images (Fig. 7B) and corresponding tumor weights (Fig. 7C) decreased significantly in the Cu-VT treated group compared to controls, $CuCl_2$, and VT groups, indicating effective tumor inhibition by Cu-VT NPs. Changes in body weight over the treatment period were monitored (Fig. 7D) to assess systemic toxicity. There was no significant weight loss in any of the treatment groups, suggesting non-interference of Cu-VT NPs in systemic toxicity. Tumor volume progression showed that Cu-VT treatment significantly inhibited tumor growth compared to other treatments and the control group (Fig. 7E). This is further supported by individual tumor growth curves (Fig. 7F), which consistently demonstrated slower tumor growth in the Cu-VT treated group. Figure 7G presents the quantified expression of caspase-3 and Ki67, respective markers of apoptosis and proliferation. The Cu-VT treated group showed significantly enhanced caspase-3 expression, indicative of enhanced apoptosis, and reduced Ki67 expression, indicating reduced cell proliferation. Immunohistochemical staining for caspase-3 and Ki67 visually confirmed these quantitative results (Fig. 7H), and more apoptotic cells and fewer proliferating cells were observed in the Cu-VT treated tumors. Additionally, ROS generation increased in the Cu-VT treated tumors (Fig. 7I). Further, DAPI/ROS staining exhibited a marked increase in ROS levels in the Cu-VT group compared to other groups. This finding corroborates the proposed mechanism of action, according to which Cu-VT NPs induce cytotoxicity through ROS-mediated oxidative stress, causing cell death.

The effect of Cu-VT NPs on apoptosis, cuproptosis, and immune response modulation in MB49 tumor tissues was examined. Immunohistochemical staining for TUNEL, FDX1, and DLAT indicated increased apoptosis and disrupted cuproptosis pathways in the Cu-VT treated group (Fig. 8A). TUNEL staining revealed DNA fragmentation, while FDX1 and DLAT are key enzymes involved in the cuproptosis pathway. The Cu-VT treated group had significantly increased TUNEL-positive cells and markedly decreased FDX1 and DLAT expression. These markers were quantified, as shown in Fig. 8B and C, further confirming the observed trends. Immunofluorescence staining for CD206/Arg-1 and CD86/iNOS revealed the repolarization of TAMs from the M2 to the M1 phenotype, as seen in Fig. 8D. CD206 and Arg-1 are M2 macrophage markers, whereas CD86 and iNOS are M1 macrophage markers. Cu-VT treatment significantly increased the proportion of M1 macrophages, indicating TAM repolarization. Flow cytometry confirmed the increase in $CD8^+$ T cell activation and TAM repolarization (Fig. 8E–G). The proportion of CD3 and CD8 double-positive T cells is presented in Fig. 8E, the dual staining for CD206 and CD86 is presented in Fig. 8F, and CD80 expression is presented in Fig. 8G. The Cu-VT treated group had significantly increased $CD8^+$ T cells and M1 macrophages. Western blot analysis of DLAT, LIAS, and FDX1 protein levels further validates the disruption of the cuproptosis pathway by Cu-VT treatment as shown in Fig. 8H. DLAT, LIAS, and FDX1 are enzymes critical to the cuproptosis pathway, and Cu-VT treatment significantly reduced their expression. The quantification of protein expression, corroborating the Western blot results is shown in Fig. 8I. These findings are consistent with the proposed mechanism which states that Cu-VT NPs induce apoptosis and cuproptosis through caspase-3 activation, GSH depletion, and ROS generation. Dying tumor cells release damage-associated molecular patterns (DAMPs), promoting the maturation of dendritic cells and activation of immune response. This leads to TAM repolarization and enhanced $CD8^+$ T cell activation, subsequently amplifying the antitumor immune response. Specifically, Cu-VT NPs directly induce cancer cell death as well as enhance antitumor immunity through immunomodulation, demonstrating significant potential for BLCA therapy.

In a BLCA mouse model, Cu-VT NPs demonstrated substantial antitumor efficacy by inhibiting tumor growth without inducing systemic toxicity. The treatment increased apoptotic markers, such as caspase-3, while reducing proliferation markers like Ki67 [45]. Additionally, Cu-VT NPs disrupted cuproptosis pathways and promoted immune modulation by repolarizing TAMs towards the M1 phenotype and enhancing $CD8^+$ T cell activation. These results highlight Cu-VT NPs as promising agents for BLCA therapy, leveraging both direct tumor cell cytotoxicity and immune response enhancement [46].

3.8 Biosafety of Cu-VT NPs

The biosafety of Cu-VT NPs was assessed through biochemical and histopathological analyses. Biochemical parameters (Supplementary Fig. 3A) such as TBIL, ALT, AST, BUN, CR, GLU, RBC, MCH, WBC, MCHC, MCV, and PLT in the Cu-VT NPs of the treated group were comparable to those of control, CuCl2, and VT groups, suggesting no significant

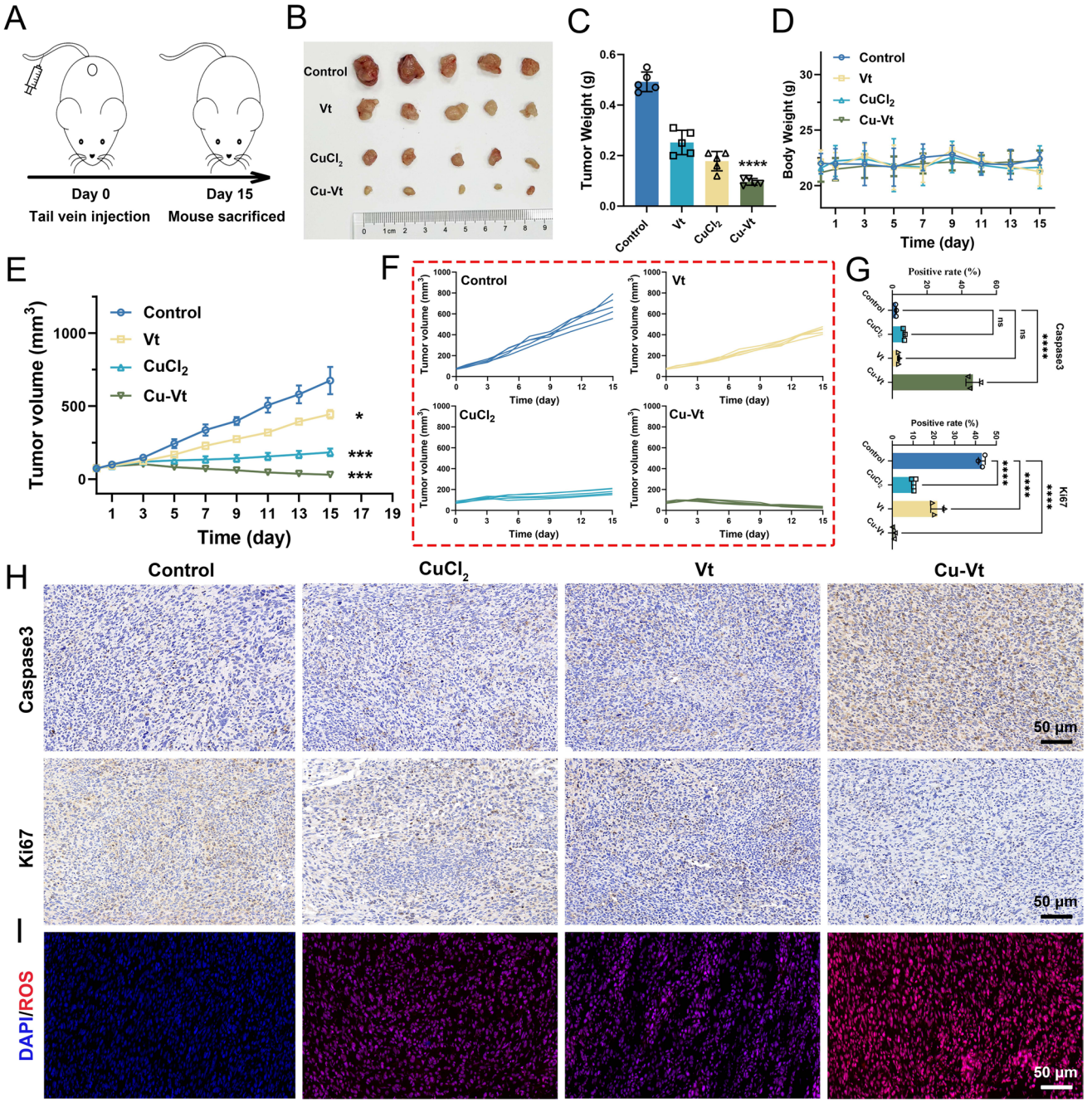

Fig. 7 In vivo efficacy of Cu-VT NPs in the mouse model of bladder cancer. **A** The schematic of the experimental design with tail vein injection and sacrifice on day 15. **B** Representative images of tumors from each treatment group. **C** Tumor weights across various groups. **D** Changes in body weight during the treatment period. **E** Tumor volume progression with time. **F** Tumor growth curves for each group. **G** Quantification of caspase-3 and Ki67 expression. **H** Immunohistochemical staining of caspase-3 and Ki67 in tumor tissues. **I** Reactive oxygen species (ROS) production in tumor tissues, demonstrated by DAPI/ROS staining. Scale bars represent 50 μm. Data are shown as mean ± standard deviation. Statistical significance is marked by $^{*}P<0.05$, $^{**}P<0.01$, $^{***}P<0.001$, and $^{****}P<0.0001$

toxicity. No noticeable tissue damage in the Cu-VT treated group was noted upon histopathological examination of major organs (Supplementary Fig. 3B) including lung, heart, liver, kidney, and spleen. These findings confirm the excellent biosafety of Cu-VT NPs.

4 Conclusion

This study demonstrates the significant potential of Cu-VT nanoparticles (NPs) in the treatment of BLCA, leveraging insights from single-cell spatial transcriptomics to design

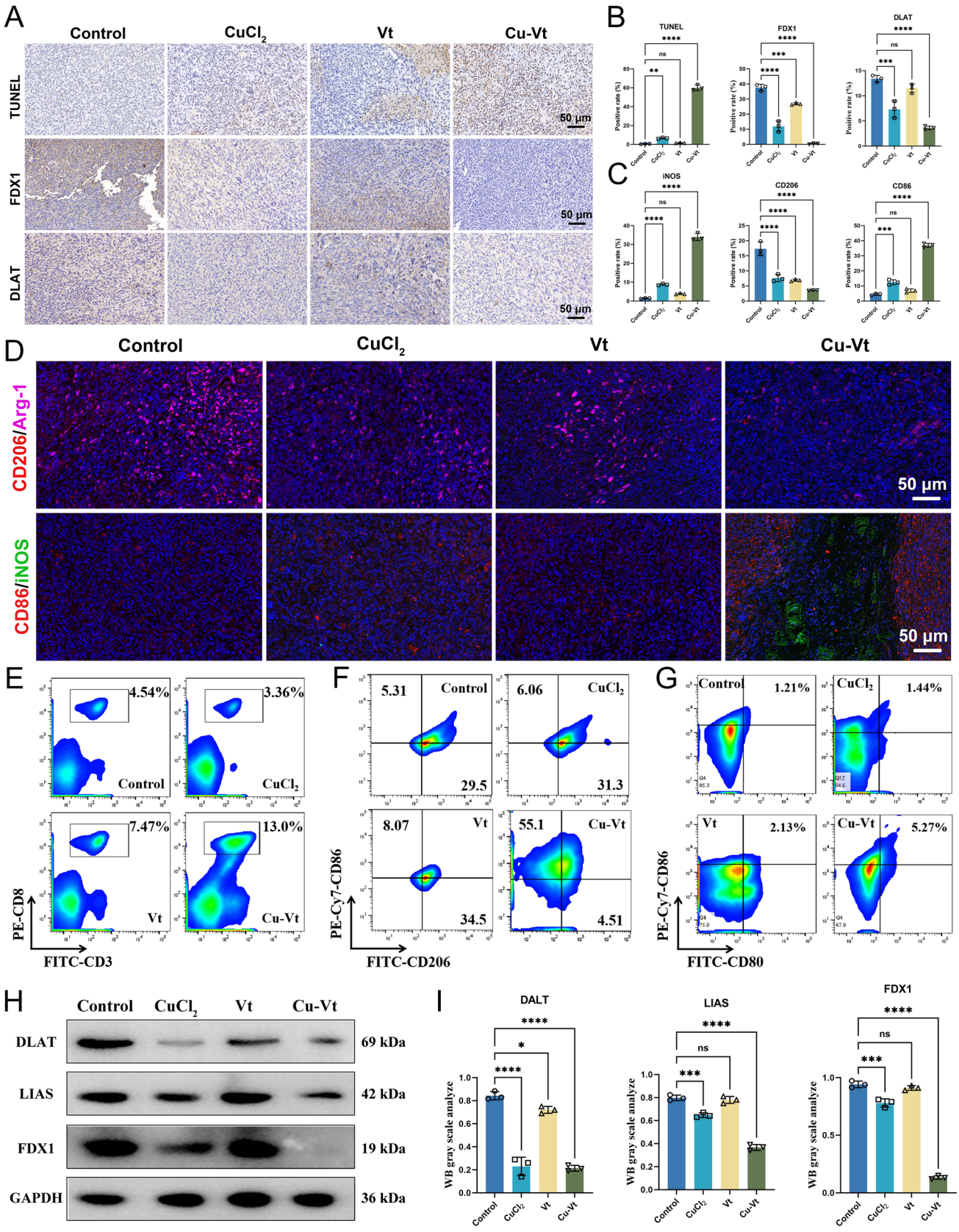
A
Control
CuCl2
Vt
Cu-Vt
TUNEL
FDX1
DLAT
50 μm
B
TUNEL
FDX1
DLAT
C
iNOS
CD206
CD86
Positive rate (%)
D
Control
CuCl2
Vt
Cu-Vt
CD206/Arg-1
CD86/iNOS
50 μm
E
4.54%
3.36%
7.47%
13.0%
Control
CuCl2
Vt
Cu-Vt
PE-CD8
FITC-CD3
F
5.31
6.06
29.5
31.3
8.07
55.1
34.5
4.51
PE-Cy7-CD86
FITC-CD206
G
1.21%
1.44%
2.13%
5.27%
FITC-CD80
H
DLAT
LIAS
FDX1
GAPDH
69 kDa
42 kDa
19 kDa
36 kDa
I
WB gray scale analyze

◂**Fig. 8** Impact of Cu-VT NPs on apoptosis, cuproptosis, and immune response in MB49 tumor tissues. **A** Immunohistochemical staining for TUNEL, FDX1, and DLAT. **B**, **C** Quantification of TUNEL, FDX1, DLAT, CD206, and CD86 expression. **D** Immunofluorescence staining for CD206/Arg-1 and CD86/iNOS. **E**–**G** Flow cytometry analysis of the expression of $CD8^+$ T cells, CD206, and CD86. **H** Western blot analysis to determine the levels of DLAT, LIAS, and FDX1 proteins. **I** Quantitative measurement of protein expression. Scale bars are set at 50 μm. Data are shown as mean ± standard deviation. Statistical significance is denoted by $^*P < 0.05$, $^{**}P < 0.01$, $^{***}P < 0.001$, $^{****}P < 0.0001$

treatments targeting cuproptosis, a key pathway in cancer pathogenesis. Cu-VT NPs were found to induce apoptosis and oxidative stress in cancer cells, concurrently modulating immune responses within the TME, leading to significantly inhibited tumor growth and reduction of lung metastasis in a mouse model. The dual mode of action, through direct cancer cell death via GSH depletion and ROS generation, and enhanced antitumor immunity through enhanced dendritic cell maturation and $CD8^+$ T cell activation, highlights their therapeutic efficacy. Additionally, the biosafety of Cu-VT NPs was confirmed, and no significant toxicity was observed in major organs and biochemical parameters. These findings suggest that Cu-VT NPs are a novel and effective therapeutic strategy for BLCA, offering improved treatment outcomes with reduced side effects, paving the way for future clinical applications.

Supplementary Information The online version contains supplementary material available at https://doi.org/10.1007/s42114-024-01153-5.

Author contribution Fangdie Ye, Chen Ye, Yufeng Zhao: original draft preparation, experimental implementation, and data processing. Haowen Jiang, Hang Huang, Xiangpeng Dai, Yufei Liu: conceptualization and supervision. Weijian Li, Jinhao Zhang, Yuxi Ou, Ziang Chen, Zhang Cheng, Jing Zhang, Shujaat Ali, Omer Salman Qureshi: methodological and material preparation.

Funding This work was supported by the National Natural Science Foundation of China (No.82373222, No.82273137), the Leading Talent Program by Shanghai Municipal Health Commission (2022LJ008), the Medical Innovation Research Special Project by Science and Technology Commission of Shanghai Municipality (22Y21900200), the Clinical Scientific and Technological Innovation Project by Shanghai Hospital Development Center (SHDC12021104), and the Fudan Institute of Urology.

Data availability The datasets used and/or analyzed during the present study are available from the corresponding author on reasonable request.

Declarations

Ethics approval and consent to participate The animal experiments were approved by the Board and Ethics Committee of Huashan Hospital, Fudan University, Approval number: 202206033S.

Conflict of interest The authors declare no competing interests.

References

1. Panebianco V, Briganti A, Boellaard TN, Catto J, Comperat E, Efstathiou J, Van Der Heijden AG, Giannarini G, Girometti R, Mertens L, Takeuchi M, Muglia VF, Narumi Y, Novara G, Pecoraro M, Roupret M, Sanguedolce F, Santini D, Shariat SF, Simone G, Vargas HA, Woo S, Barentsz J, Witjes JA (2024) Clinical application of bladder MRI and the vesical imaging-reporting and data system. Nat Rev Urol 21:243–251. https://doi.org/10.1038/s41585-023-00830-2
2. Lopez-Beltran A, Cookson MS, Guercio BJ, Cheng L (2024) Advances in diagnosis and treatment of bladder cancer. BMJ 384:e076743. https://doi.org/10.1136/bmj-2023-076743
3. Meeks JJ, Black PC, Galsky M, Grivas P, Hahn NM, Hussain SA, Milowsky MI, Steinberg GD, Svatek RS, Rosenberg JE (2023) Checkpoint inhibitors in urothelial carcinoma-future directions and biomarker selection. Eur Urol 84:473–483. https://doi.org/10.1016/j.eururo.2023.05.011
4. Dyrskjøt L, Hansel DE, Efstathiou JA, Knowles MA, Galsky MD, Teoh J, Theodorescu D (2023) Bladder cancer. Nat Rev Dis Primers 9:58. https://doi.org/10.1038/s41572-023-00468-9
5. Scilipoti P, Ślusarczyk A, De Angelis M, Soria F, Pradere B, Krajewski W, D'andrea D, Mari A, Giudice FD, Pichler R, Subiela JD, Afferi L, Albisinni S, Mertens L, Laukhtina E, Mori K, Radziszewski P, Shariat SF, Necchi A, Xylinas E, Gontero P, Rouprêt M, Montorsi F, Briganti A, Moschini M (2024) The role of mitomycin C in intermediate-risk non-muscle-invasive bladder cancer: a systematic review and Meta-analysis. Eur Urol Oncol. https://doi.org/10.1016/j.euo.2024.06.005
6. Kokorovic A, Matin SF (2020) UGN-101 (mitomycin gel): a novel treatment for low-grade upper tract urothelial carcinoma. Ther Adv Med Oncol 12:1758835920937950. https://doi.org/10.1177/1758835920937950
7. Shen YQSZH, Shen J (2019) Nanotechnology advances in medicine: focus on cancer. Eng Sci 7:1–9. https://doi.org/10.30919/es8d678
8. Boontatao P, Pannucharoenwong N, Chabuanoi T, Rattanadecho P, Tubtawee T, Panvichien S. Simulation of thermal effects on rectal wall during laser treatment of prostate cancer using hyaluronic acid and polyethylene glycol spacers: a generalized dual-phase-lag bioheat approach. Eng Sci. https://doi.org/10.30919/es1308
9. Grobet-Jeandin E, Lenfant L, Pinar U, Parra J, Mozer P, Renard-Penna R, Thibault C, Rouprêt M, Seisen T (2024) Management of patients with muscle-invasive bladder cancer with clinical evidence of pelvic lymph node metastases. Nat Rev Urol 21:339–356. https://doi.org/10.1038/s41585-023-00842-y
10. Zhang J, Zhang B, Pu C, Cui J, Huang K, Wang H, Zhao Y (2023) Nanoliposomal Bcl-xL proteolysis-targeting chimera enhances anti-cancer effects on cervical and breast cancer without on-target toxicities. Adv Compos Hybrid Mater 6:78. https://doi.org/10.1007/s42114-023-00649-w
11. Wan J, He Z, Zhao Y, Hao X, Cui J, Chen A, Zhou J, Zhang J (2023) Novel strategy of senescence elimination via toxicity-exempted kinome perturbations by nanoliposome-based thermosensitive hydrogel for osteoarthritis therapy. Adv Compos Hybrid Mater 6:104. https://doi.org/10.1007/s42114-023-00673-w
12. Caramelo B, Zagorac S, Corral S, Marqués M, Real FX (2023) Cancer-associated fibroblasts in bladder cancer: origin, biology, and therapeutic opportunities. Eur Urol Oncol 6:366–375. https://doi.org/10.1016/j.euo.2023.02.011
13. Zheng H, An M, Luo Y, Diao X, Zhong W, Pang M, Lin Y, Chen J, Li Y, Kong Y, Zhao Y, Yin Y, Ai L, Huang J, Chen C, Lin T (2024) PDGFRα+ITGA11+ fibroblasts foster early-stage cancer lymphovascular invasion and lymphatic metastasis via

ITGA11-SELE interplay. Cancer Cell 42. https://doi.org/10.1016/j.ccell.2024.02.002
14. Van De Sande B, Lee JS, Mutasa-Gottgens E, Naughton B, Bacon W, Manning J, Wang Y, Pollard J, Mendez M, Hill J, Kumar N, Cao X, Chen X, Khaladkar M, Wen J, Leach A, Ferran E (2023) Applications of single-cell RNA sequencing in drug discovery and development. Nat Rev Drug Disc 22:496–520. https://doi.org/10.1038/s41573-023-00688-4
15. Wu J, He J, Liu Z, Zhu X, Li Z, Chen A, Lu J (2024) Cuproptosis: mechanism, role, and advances in urological malignancies. Med Res Rev 44:1662–1682. https://doi.org/10.1002/med.22025
16. Feng H, Deng Z, Huang Y, Liu Z, Ruan Y, Wang T, Liu J (2023) A novel cuproptosis pattern and tumor immune microenvironment characterization in urothelial carcinoma of the bladder. Front Immunol 14:1219209. https://doi.org/10.3389/fimmu.2023.1219209
17. Xie D, Kuang Y, Yuan B, Zhang Y, Ye C, Guo Y, Qiu H, Ren J, Alshammari SO, Alshammari QA, El-Bahy ZM, Zhao K, Guo Z, Rao Q, Yang S (2025) Convenient and highly efficient adsorption of diosmetin from lemon peel by magnetic surface molecularly imprinted polymers. J Mater Sci Technol 211:159–170. https://doi.org/10.1016/j.jmst.2024.06.001
18. Rahim MA, Ejima H, Cho KL, Kempe K, Müllner M, Best JP, Caruso F (2014) Coordination-driven multistep assembly of metal–polyphenol films and capsules. Chem Mater 26:1645–1653. https://doi.org/10.1021/cm403903m
19. Chairat M, Thongsamai P, Meephun T, Pantanit S, Samosorn S, Sajomsang W, Gonil P, Bremner JB (2024) Silk dyeing with anthocyanin dye extract from Melastoma malabathricum L. fruits using metal oxides and reducing agents to ameliorate photo-fading. ES Mater Manuf 25:1213. https://doi.org/10.30919/esmm1213
20. Guo Y, Sun Q, Wu F-G, Dai Y, Chen X (2021) Polyphenol-containing nanoparticles: synthesis, properties, and therapeutic delivery. Adv Mater 33:e2007356. https://doi.org/10.1002/adma.202007356
21. Kakade SS, Bote HK, Sarvalkar PD, Sharma KKK, Pawar PK (2024) Effects of common food additives on HepG2 cells: accumulation of reactive oxygen species and induction of cell damage and death. ES Food Agrofor 17:1142. https://doi.org/10.30919/esfaf1142
22. Hao P, Yang L, Yan Y, Wang X, Yin J, Hong W, Wang S, Yin X, Liu S (2024) Metal-based nanocomposites for immunotherapy of osteosarcoma. Adv Compos Hybrid Mater 7:200. https://doi.org/10.1007/s42114-024-01030-1
23. Wang Y, Pei P, Yang K, Guo L, Li Y (2024) Copper in colorectal cancer: from copper-related mechanisms to clinical cancer therapies. Clin Transl Med 14:e1724. https://doi.org/10.1002/ctm2.1724
24 Venkatachalam H, Jayashree BS, Shrungeswara AH (2022) Evaluation of anti-inflammatory potentials of novel flavonols and their metal complexes. Eng Sci 18:217–223. https://doi.org/10.30919/es8e676
25. Liu H, Huang M, Xin D, Wang H, Yu H, Pu W (2024) Natural products with anti-tumorigenesis potential targeting macrophage. Phytomedicine 131:155794. https://doi.org/10.1016/j.phymed.2024.155794
26. Zhang R, Cheng L, Dong Z, Hou L, Zhang S, Meng Z, Betzer O, Wang Y, Popovtzer R, Liu Z (2021) Ultra-small natural product based coordination polymer nanodots for acute kidney injury relief. Mater Horiz 8:1314–1322. https://doi.org/10.1039/d0mh00193g
27. Kabdrakhmanova S, Joshy KS, Sathian A, Aryp K, Akatan K, Shaimardan E, Beisebekov M, Gulden T, Kabdrakhmanova A, Maussumbayeva A, Joseph TM, Thomas S (2023) Anti-bacterial activity of Kalzhat clay functionalized with Ag and Cu nanoparticles. Eng Sci 26:972. https://doi.org/10.30919/es972
28 Dahivade PB, Pawar SN, Pathan HM, Lokh BJ (2024) Temperature-dependent hydrothermal synthesis of CdO nanoparticles and its analysis for supercapacitor application. ES Energy Environ 24:1098. https://doi.org/10.30919/esee1098
29. Zeng X, Wang S, Peng Z, Wang M, Zhao K, Xu BB, Yin X, Ibrahim MM, GaM M, El-Bahy ZM, Guo Z, Xiang W, Wang J (2024) Rapid screening and sensing of stearoyl-CoA desaturase 1 (SCD1) inhibitors from ginger and their efficacy in ameliorating non-alcoholic fatty liver disease. J Food Meas Charact 18:6843–6857. https://doi.org/10.1007/s11694-024-02697-2
30. Zhao K, Qian C, Qi L, Li Q, Zhao C, Zhang J, Han G, Xia L, El-Bahy ZM, Gu J, Helal MH, Yan Z, Guo Z, Shi Z (2024) Modified acid polysaccharide derived from Salvia przewalskii with excellent wound healing and enhanced bioactivity. Int J Biol Macromol 263:129803. https://doi.org/10.1016/j.ijbiomac.2024.129803
31. Wang Y, Pei H, Chen W, Du R, Li J, He Z (2023) Palmatine protects PC12 cells and mice from abeta25–35-induced oxidative stress and neuroinflammation via the Nrf2/HO-1 pathway. Molecules 28. https://doi.org/10.3390/molecules28247955
32. Hu H, Zhang W, Zhou Y, Zhao K, Kuang J, Liu X, Li G, Xi Y (2024) Engineered mitochondrial ROS scavenger nanocomplex to enhance lung biodistribution and reduce inflammation for the treatment of ARDS. Adv Compos Hybrid Mater 7:194. https://doi.org/10.1007/s42114-024-00989-1
33. Justus CR, Marie MA, Sanderlin EJ, Yang LV (2023) Transwell in vitro cell migration and invasion assays. Methods Mol Biol 2644:349–359. https://doi.org/10.1007/978-1-0716-3052-5_22
34. Zhao K, Qi L, Li Q, Wang Y, Qian C, Shi Z (2024) Self-absorbing multilayer skin-like composite with Phyllostachys nigra polysaccharides promotes wound healing. Adv Compos Hybrid Mater 7:225. https://doi.org/10.1007/s42114-024-01018-x
35. Pei H, He Z, Du R, Han C, Sheng Y, Wang J, Zhou X, Li W, Cao C, Sheng J, Wang X (2023) Imidacloprid activates Kupffer cells pyroptosis to induce liver injury in mice via P2X7. Int Immunopharmacol 119:110179. https://doi.org/10.1016/j.intimp.2023.110179
36. Ma L, Chen H, Yang W, Ji Z (2023) Crosstalk between mesenchymal stem cells and cancer stem cells reveals a novel stemness-related signature to predict prognosis and immunotherapy responses for bladder cancer Patients. Int J Mol Sci 24. https://doi.org/10.3390/ijms24054760
37. Wang Y, Ju L, Wang G, Qian K, Jin W, Li M, Yu J, Shi Y, Wang Y, Zhang Y, Xiao Y, Wang X (2023) DNA polymerase POLD1 promotes proliferation and metastasis of bladder cancer by stabilizing MYC. Nat Commun 14:2421. https://doi.org/10.1038/s41467-023-38160-x
38. Zhang L, Li Y, Zhou L, Zhou H, Ye L, Ou T, Hong H, Zheng S, Zhou Z, Wu K, Yan Z, Thiery JP, Cui J, Wu S (2023) The m6A reader YTHDF2 promotes bladder cancer progression by suppressing RIG-I-mediated immune response. Can Res 83:1834–1850. https://doi.org/10.1158/0008-5472.Can-22-2485
39. Yu X, Li B, Yan J, Li W, Tian H, Wang G, Zhou S, Dai Y (2024) Cuproptotic nanoinducer-driven proteotoxic stress potentiates cancer immunotherapy by activating the mtDNA-cGAS-STING signaling. Biomaterials 307:122512. https://doi.org/10.1016/j.biomaterials.2024.122512
40. Li D, Ha E, Zhou Z, Zhang J, Zhu Y, Ai F, Yan L, He S, Li L, Hu J (2024) "Spark" PtMnIr nanozymes for electrodynamic-boosted multienzymatic tumor immunotherapy. Adv Mater 36:e2308747. https://doi.org/10.1002/adma.202308747
41. Wang R, Qiu M, Zhang L, Sui M, Xiao L, Yu Q, Ye C, Chen S, Zhou X (2023) Augmenting immunotherapy via bioinspired MOF-based ROS homeostasis disruptor with nanozyme-cascade

reaction. Adv Mater 35:e2306748. https://doi.org/10.1002/adma.202306748
42. Wang YY, Zhang XY, Li SL, Jiang FL, Jiang P, Liu Y (2023) AuPt-Loaded Cu-doped Polydopamine nanocomposites with multienzyme-mimic activities for dual-modal imaging-guided and cuproptosis-enhanced photothermal/nanocatalytic therapy. Anal Chem 95:14025–14035. https://doi.org/10.1021/acs.analchem.3c02661
43. Xie J, Yang Y, Gao Y, He J (2023) Cuproptosis: mechanisms and links with cancers. Mol Cancer 22:46. https://doi.org/10.1186/s12943-023-01732-y
44. Chen L, Min J, Wang F (2022) Copper homeostasis and cuproptosis in health and disease. Signal Transduct Target Ther 7:378. https://doi.org/10.1038/s41392-022-01229-y
45. Jung M, Rose M, Knuechel R, Loeffler C, Muti H, Kather JN, Gaisa NT (2023) Characterisation of tumour-immune phenotypes and PD-L1 positivity in squamous bladder cancer. BMC Cancer 23:113. https://doi.org/10.1186/s12885-023-10576-0
46. Xu PH, Chen S, Wang Y, Jin S, Wang J, Ye D, Zhu X, Shen Y (2023) FGFR3 mutation characterization identifies prognostic and immune-related gene signatures in bladder cancer. Comput Biol Med 162:106976. https://doi.org/10.1016/j.compbiomed.2023.106976